International Journal of Design & Nature and Ecodynamics
Vol. 19, No. 6, December, 2024, pp. 1837-1846
Journal homepage: http://iieta.org/journals/ijdne

Efficient Photocatalytic Degradation of Methylene Blue Using Magnetic $CoFe_2O_4$@CuO@Ag_3VO_4 Nanocomposite

Saja H. Al Saady*, Shahlaa Esmail Ebrahim

Environmental Engineering Department, College of Engineering, University of Baghdad, Baghdad 10070, Iraq

Corresponding Author Email: saja.hasan2311@coeng.uobaghdad.edu.iq

https://doi.org/10.18280/ijdne.190601

Received: 12 September 2024
Revised: 21 October 2024
Accepted: 12 November 2024
Available online: 27 December 2024

Keywords:
advanced oxidation process (AOP), photocatalysis, $CoFe_2O_4$@CuO@Ag_3VO_4 composite, methylene blue degradation, band gap energy

ABSTRACT

A novel magnetic photocatalyst nanocomposite, $CoFe_2O_4$@CuO@Ag_3VO_4, was effectively synthesized by integrating a co-precipitation method with a simple hydrothermal process. Various techniques were utilized to investigate the nanocomposite's structure, magnetic properties, and morphologies. Techniques such as XRD, DRS, VSM, FE-SEM, TEM, and BET were utilized. The DRS analysis determined that the band gaps of $CoFe_2O_4$, $CoFe_2O_4$@CuO, and $CoFe_2O_4$@CuO@Ag_3VO_4 NPS were 3.1, 2.82, and 2.64 eV, respectively. This study focused on the removal of organic dye methylene blue (MB dye) from wastewater to preserve water sources and aquatic organisms from toxic and carcinogenic pollutants. The effectiveness of MB dye breakdown was examined under various conditions, including varying photocatalyst dosage (0.5, 1, 2, 3) g/L, initial pollutant concentrations (10, 30, 50) ppm, H_2O_2 concentrations (0.05, 0.1 M), and pH values (2, 5, 7, 11). The objective of this work is to create an effective, low-cost, stable, and reusable substance for the treatment of wastewater. About 99.7% of the harmful organic dye (methylene blue) was removed by $CoFe_2O_4$@CuO@Ag_3VO_4 under optimal conditions (photocatalyst dosage=1g/L, MB concentration=10ppm, H_2O_2 concentration=0.1M, and pH=11). This material shows superior performance compared to other catalysts because of its narrow band gap, high magnetic saturation, lower electron/hole recombination, and high stability.

1. INTRODUCTION

Every year, large amounts of organic pollutants are discarded in water sources from several industries, such as textiles, tanning, food, plastic, and cosmetics. It is concerning that during the dyeing process, a sizable amount, (12-50)%, of these chemicals are discharged into the environment as effluent. These organic materials are very stable, but they can cause contamination of surface and groundwater if they are not treated carefully [1]. Chronic exposure to these hazardous and carcinogenic pollutants can cause irreversible harm to the environment and all living things, including humans, plants, and animals [2]. Methylene blue (MB) dye is a common cationic dye that is poisonous, carcinogenic, mutagenic, and ecologically persistent. It is extensively employed as a synthetic dye for dying fabrics in garment and textile sectors and for dyeing papers and leathers [3]. Thus, many scientists and academics are concerned about effectively managing persistent organic contaminants like dyes. Ozonation, electrochemical oxidation, chemical oxidation, adsorption, photocatalytic degradation, ion exchange, membrane separation, and biological treatments are some of the technologies that have been used to destroy MB in aqueous solutions [4-6]. Photocatalysis, a sustainable technology within the advanced oxidation process, is employed for various environmental applications, including organic degradation, microbial inhibition, cancer cell eradication, and air pollution mitigation, through the generation of diverse reactive oxygen species (ROS), such as hydroxyl radicals (•OH), superoxide radicals ($•O_2$), hydrogen peroxide (H_2O_2), along with free electrons (e-) and holes (h+). Moreover, semiconductor photocatalysis represents a highly promising and efficient technology owing to its cost-effectiveness, environmentally friendly nature, elevated degradation rate, low toxicity, ease of modification of optical and electronic characteristics, and capacity for recycling without losing photocatalytic efficacy. In addition, it requires only photoactive material and solar light (or artificial light) to completely mineralize the organic contaminants into water, CO_2, and non-hazard products [7]. Notwithstanding their efficacy, these materials experience electron/hole recombination, possess a broad bandgap energy, exhibit reduced stability, and face challenges in separating exhausted photocatalysts. These limitations can significantly undermine their reliability. Consequently, various advanced technologies and enhancements have been devised to address these issues, including nanoparticles, doping, coupling, dye sensitization, and semiconductor-semiconductor heterojunctions (e.g., supporting and core/shell composites) [8]. Recent investigations have focused on nanosemiconductors such as TiO_2, ZnO, ZnS, CdS, Fe_2O_3, $SrTiO_3$, and Ag_2WO_4 in numerous environmental purification applications, including

organic degradation, microbial inactivation, sensing, water splitting, and solar cells [9].

For instance, the flower-like $Fe_3O_4/SiO_2/MnO_2$/BiOBr-Bi magnetic composite photocatalyst was used for the degradation of methylene blue (MB), achieving a removal rate of approximately 95.23% within 180 minutes [10]. Similarly, an Au-TiO_2 catalyst degraded MB with an efficiency of 88.6%. Under visible light, Fe_2O_3 demonstrated the highest Rhodamine B (RhB) dye degradation efficiency of 94%, while the methyl orange (MO) degradation rate over CdS was 68.30% [11].

This study aims to develop an effective, low-cost, and recyclable photocatalyst for the degradation of organic pollutants (MB dye). The magnetic semiconductor material used in this work, cobalt ferrite, possesses several unique properties, including a small optical bandgap, nontoxicity, and affordability. When combined with metal oxides like CuO, cobalt ferrite's magnetic properties make it suitable for magnetic separation of materials from aqueous solutions [8]. On the other hand, Ag_3VO_4 is a silver-based photocatalyst that effectively degrades natural toxins under visible light [10, 11]. This semiconductor's ability to absorb a significant amount of solar energy makes it an ideal candidate for developing highly efficient, visible light-driven photocatalysts [12].

Table 1. Advantages and disadvantages of physical, chemical, and biological technologies used for organic degradation

Technique	Advantage	Disadvantage
Physical method	-They can be applied to remove all types of organic pollutant by adsorption and membrane filtration.	-They merely transfer the removed pollutants from one phase to another without actually destruction exhibiting secondary toxic effluent.
Chemical method	-Simple. -Efficient. -Distructive of organic pollutants.	-Expensive. -Produced large amount of sludge. -Required high quantities of chemicals.
Biological method	-Green treatment technology. -Require fewer chemicals and energy. -Harmless end product. -Low running costs.	-Inapplicable for degradation of toxic organic pollutants. -Not sufficient for TOC and COD removal. -Sensitive to environmental factores.

Table 1 shows the advantages and disadvantages of some of these techniques.

2. MATERIALS AND METHODS

2.1 Materials

Cobalt(II) nitrate [$Co(NH_3)_2.6H_2O$], iron(III) nitrate [$Fe(NO_3)_3.9H_2O$], copper acetate [$Cu(CH_3COO)_2.H_2O$], silver nitrate [$AgNO_3$], ammonium vanadate [NH_4VO_3], sodium hydroxide [NaOH], hydrochloric acid [HCl], ethanol [C_2H_5OH], hydrogen peroxide [H_2O_2], and methylene blue [$C_{16}H_{18}ClN_3S$] were used in this study. All the reagents were of analytical grade and were employed without any further purification.

2.2 Synthesis of metal ferrites photocatalysts ($CoFe_2O_4$)

From nitrate salts, the metal ferrite photocatalyst $CoFe_2O_4$ was synthesized via the co-precipitation technique. Two solutions of 100 mL distilled water containing 0.2M cobalt nitrate and the other containing 0.4M iron nitrate were combined and stirred for 30 minutes at 250 rpm using a magnetic stirrer. Incorporating 0.1M NaOH into the mixture increased the pH to (11-12). To accomplish homogenization, the mixture was heated to 80 degrees Celsius for 30 minutes and then subjected to 37 minutes of ultrasonication and 10 minutes of centrifugation at 4500 revolutions per minute [13, 14], following multiple washes with ethanol and distilled water; the combination was subjected to eight hours of drying at 80 degrees Celsius (Figure 1).

2.3 Synthesis of $CoFe_2O_4$@CuO

The steps outlined in Figure 2 were followed to synthesize $CoFe_2O_4$@CuO nanoparticles. Add 4.5 g of $CoFe_2O_4$ to 80 mL of distilled water. After a 30-minute ultrasonic mixing phase, a solution consisting of 0.5 g of copper acetate dissolved in 20 mL of distilled water was introduced into the initial solution. The resulting mixture was then agitated using a magnetic stirrer for an additional duration of 30 minutes. Drops of a 0.1M NaOH solution were utilized to lower the pH to (11-12), and it was placed in an autoclave device at 200°C for 8hr [11]. The $CoFe_2O_4$@CuO black powder was created after washing several times with water and ethanol and drying in a furnace.

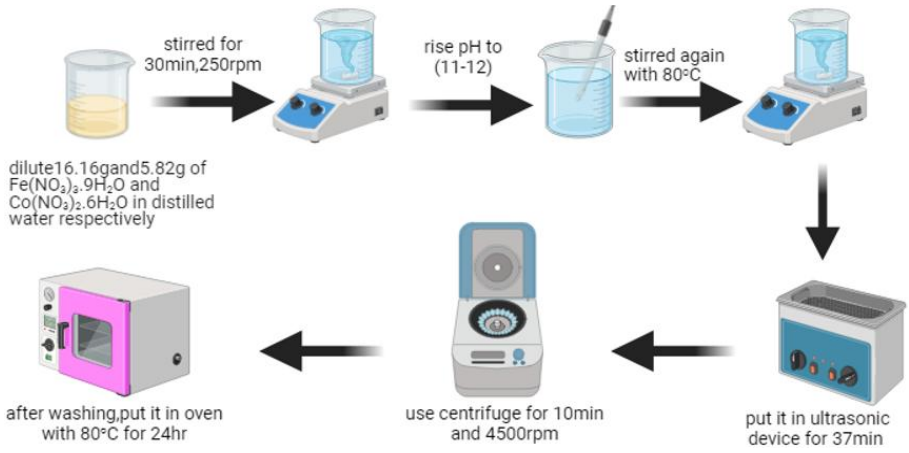

Figure 1. Steps of fabrication of $CoFe_2O_4$

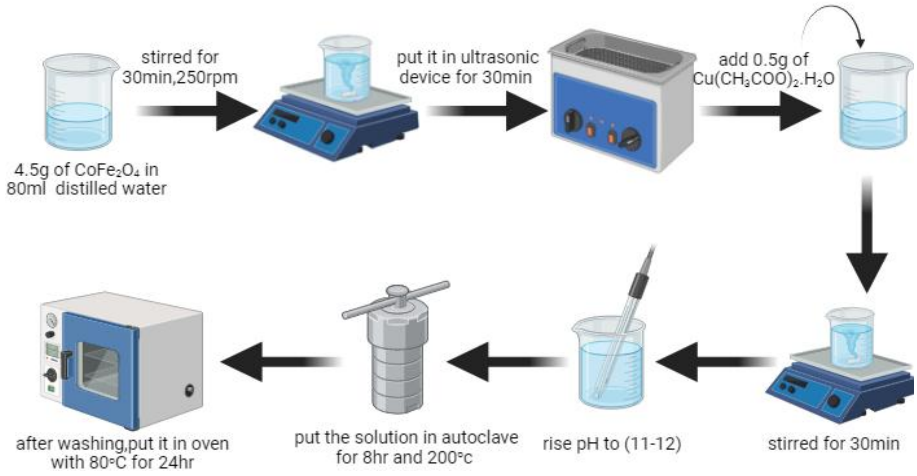

Figure 2. Synthesis of $CoFe_2O_4$@CuO

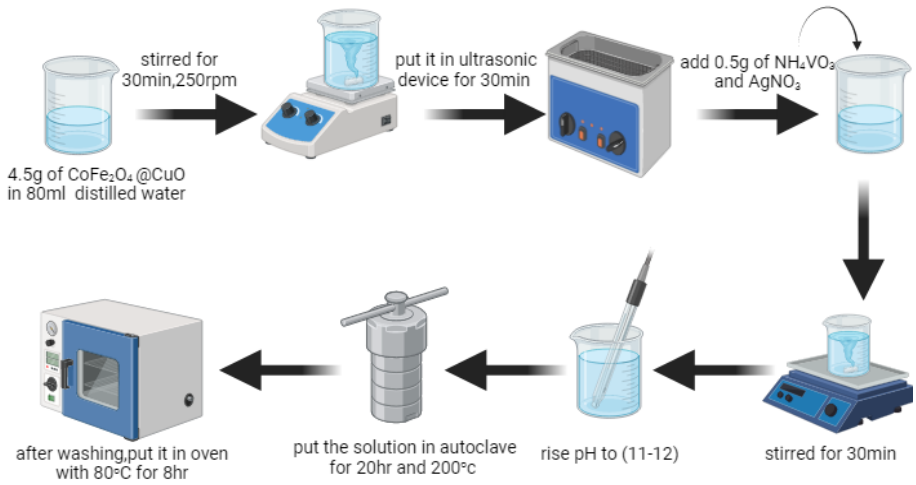

Figure 3. Fabrication of $CoFe_2O_4$@CuO@Ag_3VO_4 photocatalyst

2.4 Synthesis of $CoFe_2O_4$@CuO@Ag_3VO_4

The hydrothermal method was used to create $CoFe_2O_4$@CuO@Ag_3VO_4 nanoparticles. The weight percentages of the components were as follows: 90% $CoFe_2O_4$@CuO, 5% ammonium vanadate, and 5% silver nitrate. The solution was deemed homogenous after supervising 30 minutes of ultrasonication and 60 minutes of stirring. The pH was then brought down to 11 or 12 by adding a NaOH solution (the procedure is depicted in Figure 3). The ensuing procedures involved operating an autoclave at a temperature of 200°C for 20 hours, followed by rinsing with ethanol and distilled water, and concluding with the process of drying [13].

2.5 The characterizations of synthesized photocatalysts

Extensive imaging techniques were employed to characterize the photocatalysts obtained, including XRD, FE-SEM, VSM, TEM, BET, BJH, and UV-vis DRS. The (XRD) analysis was conducted at ambient temperature, scanning a range of 2θ values from 20° to 80° at an average speed of 2° per minute. The recently produced photocatalysts were examined for their crystallinity and chemical composition using a Shimadzu XRD-7000. A wavelength of 0.15418 nanometers characterized the graphite-chromatized radiation. The tube had an electrical current of 30 milliamperes and a voltage of 40 kilovolts. Many photocatalysts' morphology and particle size analysis were investigated using TEM (TEM, Hitachi, H-7500, Japan) and FE_SEM (FE-SEM, Tescan Mira3, France). "Vibrating sample-magnetometer" (VSM, EZ7, Microsence, Japan) was utilized to assess the magnetic characteristics of the photocatalysts. The VSM operates within a field range of -10,000 to +10,000 Oe. The photocatalysts' specific surface area and total pore volume were determined by analyzing N2 adsorption/desorption isotherms and employing the "Brunauer-Emmett-Teller" (BET) approach. Furthermore, the photocatalyst's mean pore diameter and range of pore sizes were determined using the "Barrett-Joyner-Halenda" (BJH) technique. The bandgap energy of the generated materials was evaluated using "UV-visible diffuse reflectance spectroscopy" (DRS) on the Hitachi U-3900H equipment.

2.6 The photocatalytic performance

The photocatalytic degradation effectiveness against MB dye was examined using a batch reactor consisting of a one-thousand-milliliter Pyrex beaker where the mixture occurs. As shown in Figure 4, the reactor was illuminated using a structure of visible light (VL) sources, which included four 30W xenon lamps. For the duration of the procedure, the photocatalysts were suspended in a mixture of MB dye and water. In the initial experiment, a one-hundred-milliliter

solution of MB dye was equipped using a 0.1M H_2O_2 solution, a naturally occurring pH, 0.5 g/L of photocatalysts created, and a starting concentration of 10 ppm. The absorption-desorption equilibrium state was reached after 60 minutes of constant stirring in the dark control [14]. Afterwards, the MB dye was photocatalytically destroyed by exposing the reactor to visible light for 90 minutes. It determined the residual MB concentration using a 595 nm UV-spectrometer by taking two milliliters of the deteriorated sample every fifteen minutes. Eq. (1) was used to compute the photocatalysts' degradation performance (DP) [12]:

$$DP(\%)=(C_0 - C_t)/C_0 \times 100 \quad (1)$$

where, C_0 is the initial concentration (10ppm), and C_t is the final concentration of MB solution after photocatalysis process.

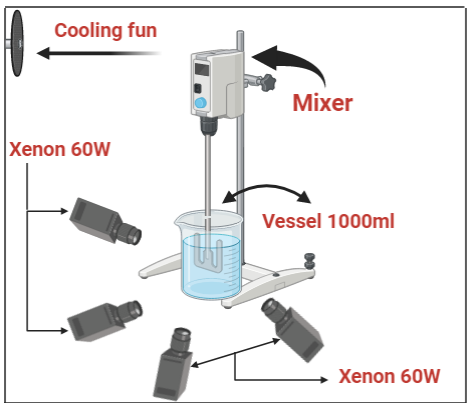

Figure 4. The batch photoreactor is used in the photocatalysis process

3. RESULTS AND DISCUSSION

3.1 Characteristics results

3.1.1 Photocatalysts phase analysis

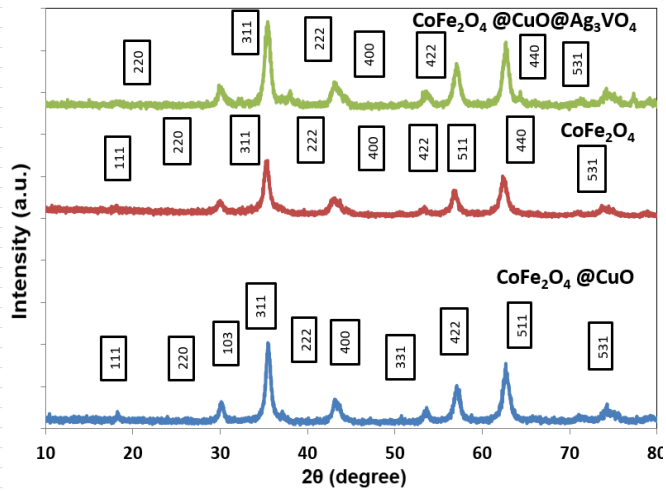

Figure 5. The XRD diffraction patterns of synthesized photocatalysts

Figure 5 shows the XRD pattern of spinel-type cobalt ferrite nanoparticles made at 300 K room temperature using the sol-gel auto-combustion procedure.

Particularly striking in the XRD pattern are several reflections, namely (220), (311), (222), (400), (422), (511), and (440). The peaks are indexed based on the JCPDS card number 22-1086. Here, the F.C.C. cubic structure's reflections can observe. For XRD purposes, these reflections are the only peaks. The crystallite size was 21.6 nm by utilizing the most prominent peak (311 in this case) and the famous Scherrer's formula. The (220), (311), (422), (511), and (440) planes of a cubic structure $CoFe_2O_4$ are thought to be responsible for the visible peaks, according to standard data (JCPDS card no. 22-1086). Two reflections at 2θ =35.3 (002) and 2θ =39 (111) probably formed the monoclinic crystal phase of CuO, as shown by the diffraction patterns. Applying the Deby-Scherrer equation to the XRD data, it found that the peak with the maximum intensity was about 36 nanometers, which is the estimated crystallite size. Peaks at 311 are observed for both the $CoFe_2O_4$@CuO and $CoFe_2O_4$ components in the composite $CoFe_2O_4$@CuO@Ag_3VO_4 [15].

3.1.2 Optical properties of synthesized photocatalysts

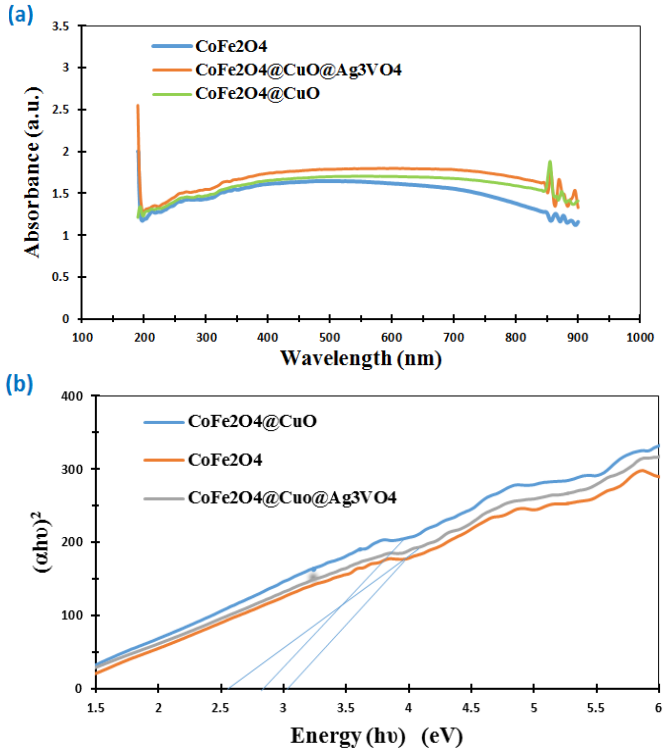

Figure 6. The optical properties of photocatalysts (a) UV-vis DRS analysis (b) Optical bandgap using Tauc plots of $(\alpha h\nu)^2$ versus hν for photocatalysts

Figure 6(a) displays the results of the UV-vis DRS study that investigated the VL absorption boundaries and "band gap energy" (Eg) of the synthesized photocatalyst. The $CoFe_2O_4$@CuO@Ag_3VO_4 sample showed wide absorption boundaries in the VL region and excellent absorption in the ultraviolet and VL spectra. Its absorption edge value was 350 nm. Expanding heteroconnections between CuO and Ag_3VO_4 NPs broaden absorption boundaries. This attribute can augment the photocatalytic efficacy of the composite material in comparison to $CoFe_2O_4$ and $CoFe_2O_4$@CuO. This is achieved by facilitating sufficient spatial segregation of the photogenerated electron/hole (e^-/h^+) pairs upon exposure to visible light [16]. The bandgap energy (Eg) of the synthesized

samples was determined using Eq. (2), incorporating the data obtained from DRS analysis and the Kubelka-Munk relation. In this equation, α, v, h, n, and A represent the absorption coefficient, photon frequency, Planck constant, trajectory of transition, and proportionality constant, respectively [17]. The $CoFe_2O_4$@CuO samples exhibited a bandgap value of 2.82 eV, while the $CoFe_2O_4$@CuO@Ag_3VO_4 samples had a bandgap value of 2.64 eV (Figure 6(b)).

$$\alpha h\upsilon = A(h\upsilon - Eg)^{n/2} \quad (2)$$

The $CoFe_2O_4$@CuO@Ag_3VO_4 composite has better photocatalytic activity because of its low recombination rate, high electron/hole pair production rate, and lower band gap energy [18].

3.1.3 The magnetic properties of photocatalysts

By employing VSM analysis, the magnetic characteristics of the produced photocatalysts were investigated. See the magnetic hysteresis curves of the produced photocatalysts in Figure 7. For the $CoFe_2O_4$ sample, the highest magnetization saturation (MS) value was 39.9 emu/g. When the $CoFe_2O_4$ core was coated with copper oxide, the core/shell combination reduced this value to 38.3 emu/g. After adsorbing Ag_3VO_4 onto the surface of $CoFe_2O_4$@CuO MNCs, the MS value dropped to 33.7 emu/g. The outcome is due to a drop in the $CoFe_2O_4$ weight ratio [6]. Because the produced photocatalysts are magnetic, separating them after treatment by applying an external magnet is simple.

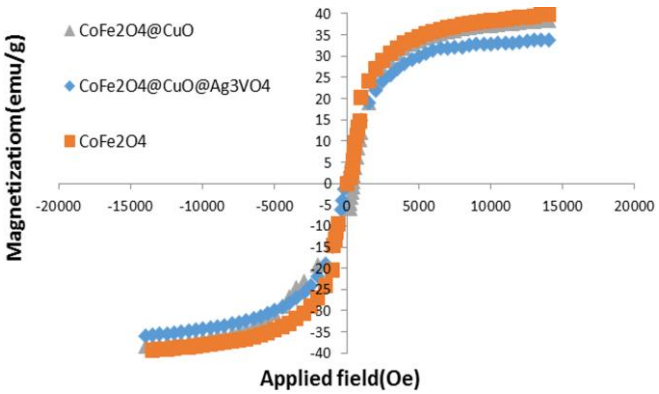

Figure 7. Magnetic hysteresis curves of synthesized photocatalysts

3.1.4 Morphology analysis

The optical characteristics of the produced photocatalysts were examined using (FE-SEM). The (SEM) of $CoFe_2O_4$, shown in Figure 8(a), shows a fractured structure with microsphere clusters 200–400 nm diameter. The grain diameters of these nanoparticles vary between fourteen and forty-seven nanometers. The tiny quantity of aggregation seen was generated by the magnetic characteristics and instability of the $CoFe_2O_4$ NPs [4]. Figure 8(b) shows that the $CoFe_2O_4$@Cuo picture revealed a nanoparticle structure free of aggregates. Copper oxide coating $CoFe_2O_4$ NPs reduces their instability and magnetic saturation value, which may explain the result.

By looking at the changes in cluster and particle sizes after adding Ag_3vo_4, as shown in Figure 8(c), the $CoFe_2O_4$@CuO@ Ag_3vo_4 was successfully formed. The TEM image of the Ag3vo4 sample doped with $CoFe_2O_4$@CuO is displayed in Figure 8(d). Dark and coarse, magnetite's iron oxide core is a fascinating mineral. The surface of the $CoFe_2O_4$ NPs is covered with a gray CuO shell around 20-30 nm thick. Surface images of Ag_3VO_4 shells with a thickness of about (15-20) nm are shown by $CoFe_2O_4$@CuO MNCs.

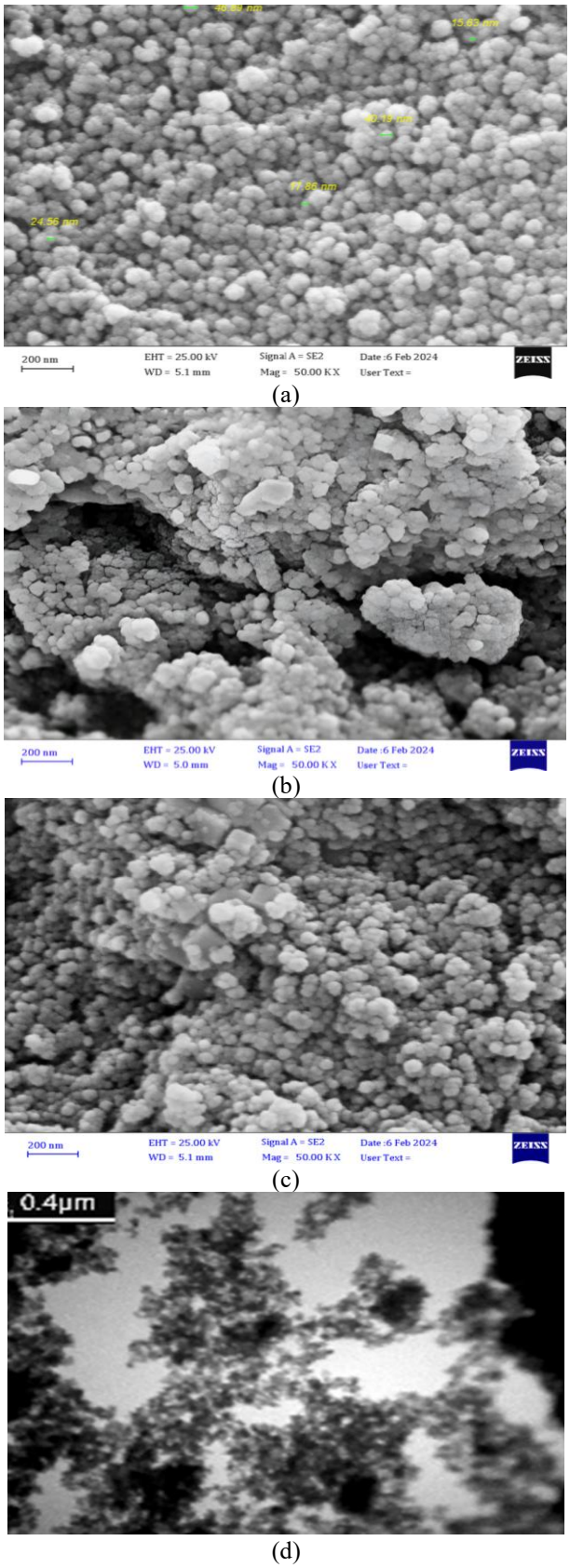

Figure 8. The FESEM for (a) $CoFe_2O_4$, (b) $CoFe_2O_4$@CuO, (c) $CoFe_2O_4$@CuO@Ag_3VO_4, and (d) TEM image for $CoFe_2O_4$@CuO@Ag_3VO_4 composites

Figure 9 displays the outcomes of determining the particular area of surface and total pore volume of MNCs by utilizing the BET analysis and "N2 adsorption/desorption" isotherms. The $CoFe_2O_4$@CuO@Ag_3VO_4 MNCs exhibited a specific surface area of 72.5 m^2/g and a total pore volume of 0.44 cm^3. Based on the data, this multinational corporation can provide an adequate number of active sites for photocatalytic removal. Using the BJH method, the typical pore size of MNCs was determined. A larger pore size value of 24.4 nm identifies the CuO mesopore structure. All of the results lined up with study [19].

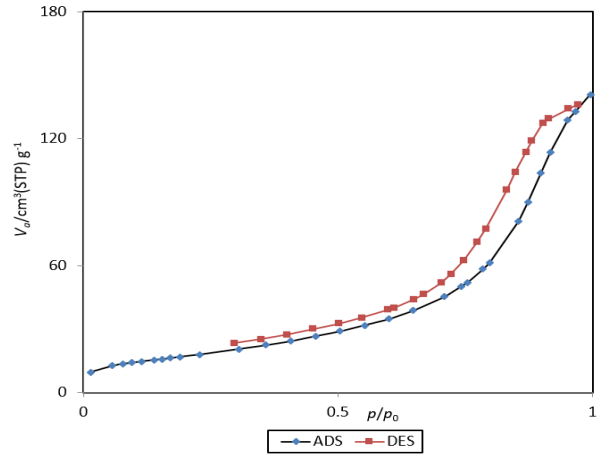

(a)

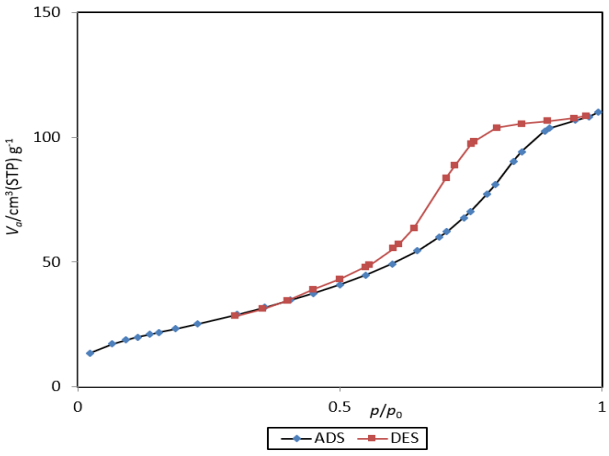

(b)

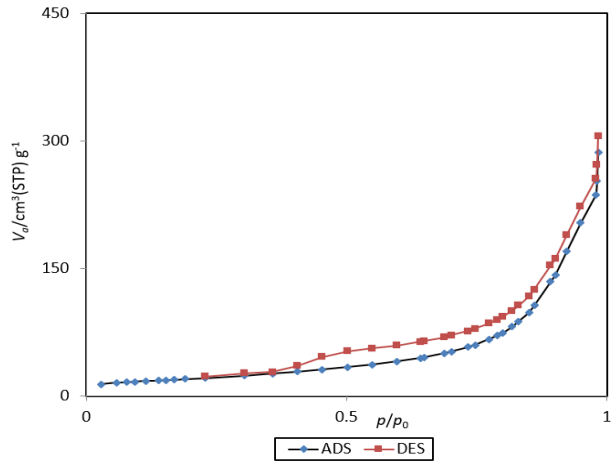

(c)

Figure 9. The adsorptions-desorption and pore size for (a) $CoFe_2O_4$, (b) $CoFe_2O_4$@CuO, and (c) $CoFe_2O_4$@CuO@Ag_3VO_4 nanocomposites

3.2 Effect of operating conditions

3.2.1 Effect of catalyst loading

The degradation rate and photocatalytic reaction are significantly affected by the amount of photocatalyst that is used. Figure 10 displays the results of an experiment that investigated the effects of different loadings (0.5, 1, and 2) g/L of $CoFe_2O_4$@CuO@Ag_3VO_4 on the photo-oxidation of MB at a level of ten milligrams per liter and pH of 7 were tested. The photodegradation efficiency increased from 91.1% to 97.7% when 0.5g and 1g of photocatalyst were used, respectively, and it decreased with increasing the photocatalyst dosage to 2g and 3g. Although there were more active sites and reactive radicals created, these data showed that increasing the loading to 2g/L and 3g/L helped inhibit the photo-reaction. However, this might trap MB molecules and drive the degrading reaction [20]. The reactor's capacity to absorb light is constrained by turbidity and aggregation effects. Therefore, the optimal concentration for MB oxidation was determined to be 1g/L of $CoFe_2O_4$@CuO@Ag_3VO_4.

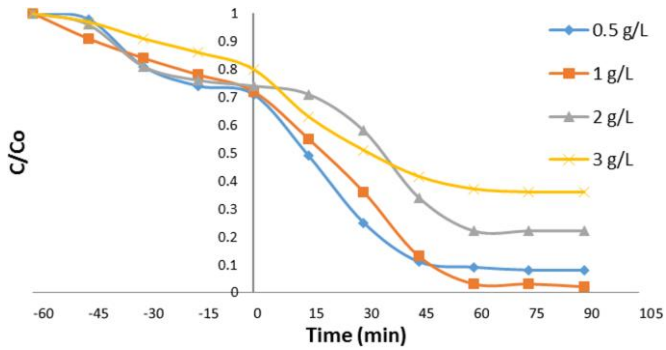

Figure 10. The influence of photocatalyst loading with operating conditions of C_o = 10ppm, H_2O_2 = 0.1M, and PH = 7

3.2.2 The effect of MB concentration

The degradation of MB concentrations (10, 30, and 50 mg/L) over $CoFe_2O_4$@CuO@Ag_3VO_4 (1 g/L, pH = 7, and H_2O_2 = 0.1M) under xenon illumination was studied to determine the effect of pollutant concentrations on MB photo-destruction. In Figure 11, it can be noticed that the removal efficiency was considerably reduced when the initial MB dye concentration was raised from 10 to 30 ppm and from 30 to 50 ppm while maintaining the same dosage of photocatalyst. This happens because higher concentrations of MB dye cause less visible light to diffuse through the solution. Because of the overload on active sites, less ROS would be created [21].

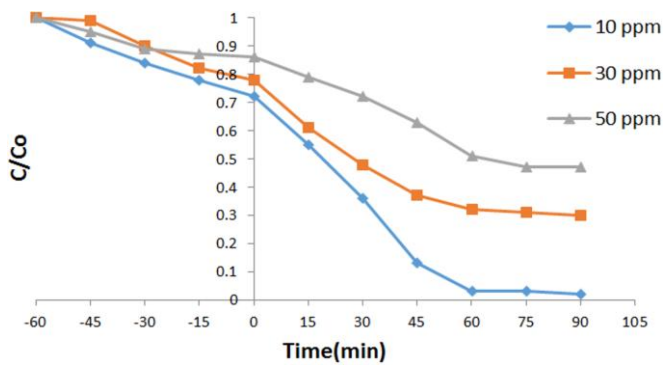

Figure 11. The influence of MB concentration on the degradation efficiency with operating conditions of dosage = 1g/L, H_2O_2 = 0.1M, and pH = 7

3.2.3 The addition of H_2O_2

0.05M and 0.1M were used to study the effect of H_2O_2 concentration on MB dye degradation efficiency with the operating conditions of (C_o = 10ppm, photocatalyst dosage = 1g/L, and pH = 7). Only 50.3% of MB dye was removed from the solution when H_2O_2 was not used after 90 minutes of visible light irradiation. In comparison, the degradation efficiency reached 76.4% when 0.05M of H_2O_2 was used within the same period. It increased furthermore until it reached 97.1% when the concentration of H_2O_2 increased to 0.1M (as shown in Figure 12). This is due to the ability of H_2O_2 to trap the electrons and create two hydroxyl radicals ($H_2O_2 \rightarrow 2^{\bullet}OH$) as well as it is sufficient oxidant to directly degrade the dye pollutant through the suspension of photocatalyst/MB with H_2O_2 [22]. Thereby, the high amount of hydroxyl radicals will accelerate the photocatalytic degradation of MB dye.

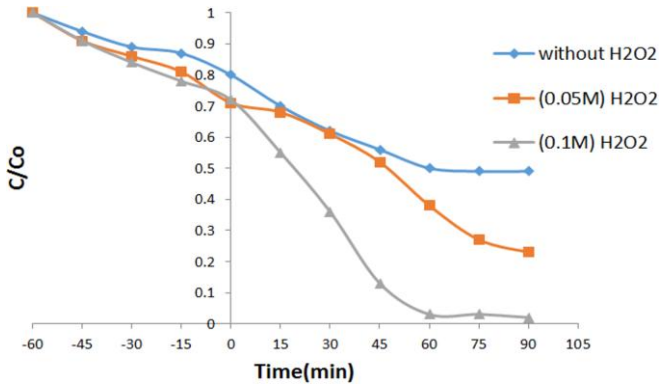

Figure 12. The effect of H_2O_2 concentration on the degradation efficiency of MB with operating conditions of (dosage = 1g/L, C_o = 10ppm, and pH = 7)

3.2.4 The effect of pH

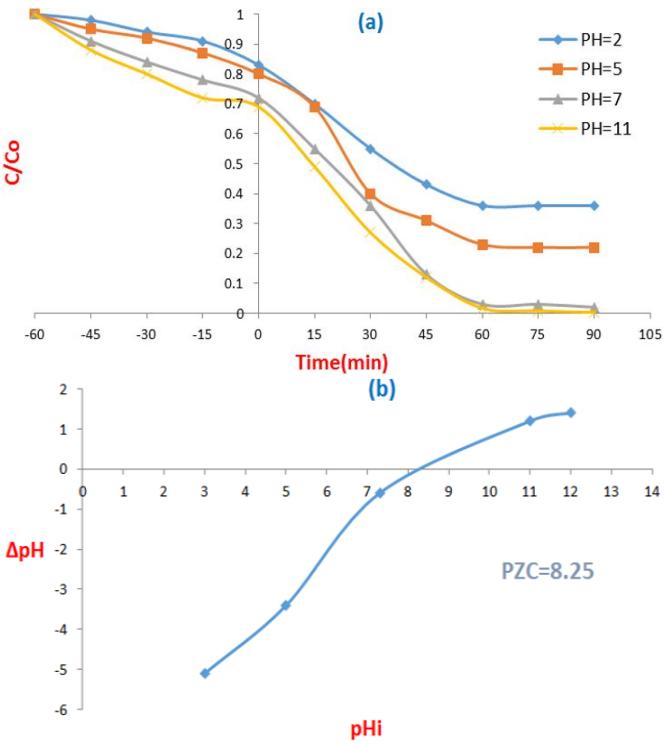

Figure 13. (a) The effect of pH solution on the photocatalytic degradation activity of MB dye, (b) The point of zero charge (PZC) for $CoFe_2O_4$@CuO@Ag_3VO_4

The solution's pH is one of the most important variables affecting the photocatalytic degradation effectiveness. It is tested in a controlled setting using 10 ppm MB dye, 1 g/L photocatalyst, and 0.1M H_2O_2 over a pH range of 2, 5, 7, and 11. Figure 13(a) shows that at pH=11, the degradation efficiency was 99.7%, and at pH=7, it decreased to 97.1%. At low pH values (2 and 5), 64% and 77.9% of the pollutants were eliminated after 90 minutes of VL irradiation, respectively. In theory, when the pH of a solution is low, the surface of the photocatalyst will have a net positive charge, and when the pH is high, the surface will have a negative charge. Using the salt-added approach [23], the photocatalysts' point of zero charge (PZC) was found to be 8.25, as illustrated in Figure 13(b). At pH values higher than 8.25, a cationic dye known as MB dye has an enhanced adsorption rate on catalyst surfaces [24, 25]. More hydroxide ions (OH) are formed at higher pH levels, which speeds up the breakdown of MB dye. These ions can react with holes to produce hydroxyl radicals [26].

4. REUSABILITY AND STABILITY STUDIES

By exposing the nanocomposite to visible light for five consecutive deterioration cycles culminating in MB, it can examine its durability and reusability. Following each run, the MB dye solution was filtered to remove the utilized photocatalyst, which was then washed several times with ethanol and distilled water and separated by using a magnetic medium. With each running cycle, the removal efficiency of $CoFe_2O_4$@CuO@Ag_3VO_4 decreased due to the catalyst mass being lowered during washing and magnetic separation after each running cycle (Figure 14); the photocatalyst's adsorption capability may diminish due to the accumulation of irreversible adsorbate, which is MB dye that cannot be fully eliminated by washing with ethanol [15]. Even if the photocatalytic degradation efficiency drops after five runs, the material is still useful due to its removal efficiency of around 78%.

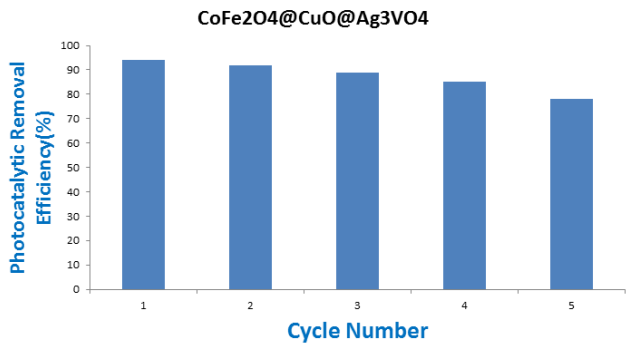

Figure 14. Reusability and stability studies of synthesized photocatalysts for five running cycles at MB dye concentration = 10 ppm, photocatalyst dosage = 1 g/L, running time = 90 min, and pH = 7

5. SCAVENGER EXPERIMENTS

To find out how each reactive species ($^{\bullet}OH$, $^{\bullet}O_2^-$, H_2O_2, e^-, h^+) contributes to the visible light photodegradation of MB dye, a set of scavenging experiments were carried out using a $CoFe_2O_4$@CuO@Ag_3VO_4 photocatalyst. The compounds utilized for collecting h^+, e^-, H_2O_2, $^{\bullet}O_2-$, and $^{\bullet}OH$ were

"Sodium oxalate, potassium dichromate, Fe(II)-EDTA, P-benzoquinone, and isopropanol". The degradation activity of MB dye was significantly reduced by sodium oxalate and "Fe (II)-EDTA," suggesting that h^+ and H_2O_2 are the primary oxidants involved in photodegradation (Figure 15). An additional setback is that isopropanol has a high removal efficiency (about 90%) following addition, further ruling out the idea that $^{\bullet}OH$ is connected to photocatalytic degradation. The influence of "reactive species in photocatalytic activity can be ordered from higher to lower values: $H_2O_2 > h^+ > e^- > {}^{\bullet}O_2^- > {}^{\bullet}OH$. The results show that the bare materials (CuO, Ag_3VO_4, and $CoFe_2O_4$) migrate VB electrons to the CB as part of the photocatalytic mechanism using the photon energy from xenon light (Figure 16). Additionally, it was discovered that pure $CoFe_2O_4$ has (Eg) of 2.7 eV, CuO has an Eg of 1.4 eV, and Ag_3VO_4 has an Eg of 2.2 eV. With the use of Eqs. (3)-(5) [12], the E_{VB} and E_{CB} values can be roughly calculated.

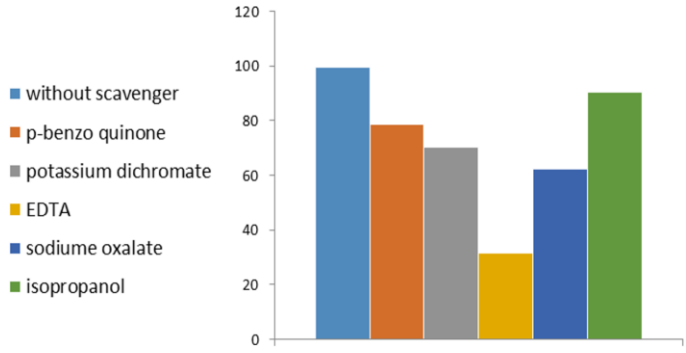

Figure 15. The photocatalytic degradation activity of $CoFe_2O_4$@CuO@Ag_3VO_4 against MB dye in the presence of different scavengers (photocatalyst dosage = 1 g/L, MB dye initial concentration = 10 ppm, initial pH = 7, running time = 90 min and H_2O_2 concentration = 0.1 M)

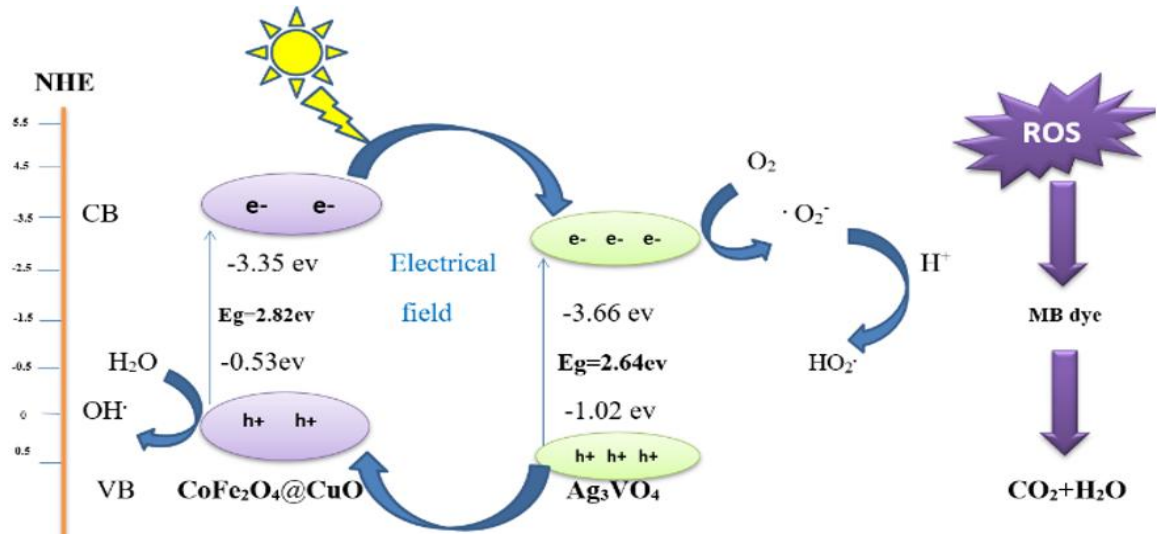

Figure 16. The mechanisms of M.B dye degradation by $CoFe_2O_4$@CuO@Ag_3VO_4

$$E_{VB} = X - E_e + 0.5Eg \quad (3)$$

$$E_{CB} = E_{VB} - Eg \quad (4)$$

$$X\,(A_mB_nC_t) = (X_A{}^m\, X^n{}_B\, X_C{}^t)^{(1/m+n+t)} \quad (5)$$

E_e stands for the free electron energy on the hydrogen scale, which is 4.5 eV, and (m, n, t) denotes the moles of each element. The elements in this case are A, B, and C. As an absolute electronegativity, X is the Pearson value. Eg band gap energy [27-37]. Because of the discrepancy in potential band energy, the released electrons can travel from the CuO CB to the Ag_3VO_4 CB, and the holes in the CuO VB can move to the Ag_3VO_4 VB. After hole production, it either oxidizes MB dye directly or reacts with adsorbed H_2O/OH- ions to produce hydroxyl radicals (Eq. (8)). Finally, as shown in Eq. (9), the M.B. dye is oxidized by a combination of oxygen, hydroxyl radicals, hydrogen peroxide, and holes, leading to the production of CO_2 and H_2O, among other byproducts.

$$CoFe_2O_4@CuO@Ag_3VO_4 + h\gamma\ (\text{visible light}) \rightarrow CoFe_2O_4@CuO@Ag_3VO_4\ (e_{CB}\text{-}+h\gamma B+) \quad (6)$$

$$e_{CB}{}^- + O_2 \rightarrow {}^{\bullet}O_2^- \quad (7)$$

$$H^+ + {}^{\bullet}O_2^- \rightarrow {}^{\bullet}OOH \rightarrow {}^{\bullet}O \quad (8)$$

$$\text{M.B dye} + {}^{\bullet}O_2^- / {}^{\bullet}OH / h\gamma B^+ \rightarrow \text{degradation} \quad (9)$$

6. CONCLUSIONS

Thoroughly produced by the hydrothermal method, the magnetic nanocomposite ($CoFe_2O_4$@CuO@Ag_3VO_4) was characterized by "XRD, DRS, FE-ESM, TEM, BET, and VSM," among other methods. The key findings from this analysis are summarized as follows:

1. The Eg of $CoFe_2O_4$ MNC was estimated to be 3.1 eV, and it reduced to 2.64 when the MNC was coated with CuO and Ag_3VO_4.
2. 99.7% of Methylene blue dye was degraded after treatment with $CoFe_2O_4$@CuO@Ag_3VO_4, which boosts its cost-effectiveness and opens up other applications with low activity loss.
3. $CoFe_2O_4$@CuO@Ag_3VO_4 has good activity in removing MB dye from wastewater even after using for several times.
4. Recommendation for future studies that use $CoFe_2O_4$@CuO@Ag_3VO_4 to remove other pollutants (organic, inorganic, and microorganisms) from wastewater and investigate the effect of more conditions such as light intensity, light type, and temperature on the removal efficiency of this MNC.

ACKNOWLEDGMENTS

Environmental Engineering Department/University of Baghdad- College of Engineering for their help in laboratory work and technical support.

REFERENCES

[1] Fuziki, M.E.K., Brackmann, R., Dias, D.T., Tusset, A.M., Specchia, S., Lenzi, G.G. (2021). Effects of synthesis parameters on the properties and photocatalytic activity of the magnetic catalyst $TiO_2/CoFe_2O_4$ applied to selenium photoreduction. Journal of Water Process Engineering, 42: 102163. https://doi.org/10.1016/j.jwpe.2021.102163

[2] Lam, S.M., Sin, J.C., Mohamed, A.R. (2016). A review on photocatalytic application of g-C_3N_4/semiconductor (CNS) nanocomposites towards the erasure of dyeing wastewater. Materials Science in Semiconductor Processing, 47: 62-84. https://doi.org/10.1016/j.mssp.2016.02.019

[3] Oladoye, P.O., Ajiboye, T.O., Omotola, E.O., Oyewola, O.J. (2022). Methylene blue dye: Toxicity and potential elimination technology from wastewater. Results in Engineering, 16: 100678. https://doi.org/10.1016/j.rineng.2022.100678

[4] Lu, Q., Wei, Z., Li, C., Ma, J., Li, L. (2022). Photocatalytic degradation of methyl orange by noble metal Ag modified semiconductor Zn_2SnO_4. Materials Science in Semiconductor Processing, 138: 106290. https://doi.org/10.1016/j.mssp.2021.106290

[5] Kyere-Yeboah, K., Bique, I.K., Qiao, X.C. (2023). Advances of non-thermal plasma discharge technology in degrading recalcitrant wastewater pollutants. A comprehensive review. Chemosphere, 320: 138061. https://doi.org/10.1016/j.chemosphere.2023.138061

[6] Jabbar, Z.H., Ebrahim, S.E. (2022). Recent advances in nano-semiconductors photocatalysis for degrading organic contaminants and microbial disinfection in wastewater: A comprehensive review. Environmental Nanotechnology, Monitoring & Management, 17: 100666. https://doi.org/10.1016/j.enmm.2022.100666

[7] Uduma, R.C., Oguzie, K.L., Chijioke, C.F., Ogbulie, T.E., Oguzie, E.E. (2023). Bioelectrochemical technologies for simultaneous treatment of dye wastewater and electricity generation: a review. International Journal of Environmental Science and Technology, 20(9): 10415-10434. https://doi.org/10.1007/s13762-022-04753-0

[8] Niu, Y.T., Guo, G.B. (2020). Synthesis, characterization, and photocatalytic activities of $BiVO_4$ by carbon adsorption hydrothermal method. Zeitschrift für anorganische und allgemeine Chemie, 646(20): 1661-1665. https://doi.org/10.1002/zaac.202000141

[9] Wang, C., Zhu, W., Xu, Y., Xu, H., et al. (2014). Preparation of TiO_2/g-C_3N_4 composites and their application in photocatalytic oxidative desulfurization. Ceramics International, 40(8): 11627-11635. https://doi.org/10.1016/j.ceramint.2014.03.156

[10] Zang, Y., Li, L., Li, X., Lin, R., Li, G. (2014). Synergistic collaboration of g-C3N4/SnO2 composites for enhanced visible-light photocatalytic activity. Chemical Engineering Journal, 246: 277-286. https://doi.org/10.1016/j.cej.2014.02.068

[11] Jabbar, Z.H., Ebrahim, S.E. (2021). Synthesis, characterization, and photocatalytic degradation activity of core/shell magnetic nanocomposites (Fe_3O_4@ SiO_2@ Ag_2WO_4@ Ag2S) under visible light irradiation. Optical Materials, 122: 111818. https://doi.org/10.1016/J.OPTMAT.2021.111818

[12] Danish, M., Muneer, M. (2021). Excellent visible-light-driven Ni-ZnS/g-C3N4 photocatalyst for enhanced pollutants degradation performance: Insight into the photocatalytic mechanism and adsorption isotherm. Applied Surface Science, 563: 150262. https://doi.org/10.1016/j.apsusc.2021.150262

[13] Jasim, N.A., Ebrahim, S.E., Ammar, S.H. (2023). A comprehensive review on photocatalytic degradation of organic pollutants and microbial inactivation using Ag/$AgVO_3$ with metal ferrites based on magnetic nanocomposites. Cogent Engineering, 10(1): 2228069. https://doi.org/10.1080/23311916.2023.2228069

[14] Hakimyfard, A., Mohammadi, S. (2019). ZnFe2O4 and ZnO-Zn1− xMxFe2O4+ δ (M= Sm3+, Eu3+ and Ho3+): Synthesis, physical properties and high performance visible light induced photocatalytic degradation of malachite green.Advanced Powder Technology, 30(6): 1257-1268. https://doi.org/10.1016/j.apt.2019.04.005

[15] Shen, X., Yang, J., Zheng, T., Wang, Q., et al. (2020). Plasmonic Pn heterojunction of Ag/Ag2S/Ag2MoO4 with enhanced Vis-NIR photocatalytic activity for purifying wastewater. Separation and Purification Technology, 251: 117347. https://doi.org/10.1016/j.seppur.2020.117347

[16] Akaood, M.A., Ali, I.M., Waisi, B.I. (2024). Water treatment performance of PAN/HPMC/Gr Nano composites. Iraqi Journal of Physics, 22(1): 42-52. https://doi.org/10.30723/ijp.v22i1.1175

[17] Qin, C., Li, H., Zhong, J., Li, J., Huang, S., Ma, L. (2021). Preparation of cypress leave-like $Ag_2WO_4/BiVO_4$ heterojunctions with remarkably enhanced photocatalytic activity. Materials Letters, 283: 128793. https://doi.org/10.1016/j.matlet.2020.128793

[18] Jing, H.P., Wang, C.C., Zhang, Y.W., Wang, P., Li, R. (2014). Photocatalytic degradation of methylene blue in ZIF-8. RSC Advances, 4(97): 54454-54462. https://doi.org/10.1039/C4RA08820D

[19] Yang, Y., Li, X., Zhou, C., Xiong, W., Zeng, G., et al. (2020). Recent advances in application of graphitic carbon nitride-based catalysts for degrading organic contaminants in water through advanced oxidation processes beyond photocatalysis: A critical review. Water Research, 184: 116200. https://doi.org/10.1016/j.watres.2020.116200

[20] Jabbar, Z.H., Ebrahim, S.E. (2021). Highly efficient visible-light-driven photocatalytic degradation of organic pollutants by using magnetically separable supported heterogeneous nanocomposites ($SiO_2/Fe_3O_4/Ag_2WO_4$). Environmental Nanotechnology, Monitoring & Management, 16: 100554. https://doi.org/10.1016/J.ENMM.2021.100554

[21] Sreedharan, A., Ong, S.T. (2020). Combination of Plackett Burman and response surface methodology experimental design to optimize malachite green dye removal from aqueous environment. Chemical Data Collections, 25: 100317. https://doi.org/10.1016/j.cdc.2019.100317

[22] Zhu, Z., Zhou, F., Zhan, S. (2020). Enhanced antifouling property of fluorocarbon resin coating (PEVE) by the modification of g-C_3N_4/Ag_2WO_4 composite step-scheme photocatalyst. Applied Surface Science, 506: 144934. https://doi.org/10.1016/j.apsusc.2019.144934

[23] Jiao, Y., Han, D., Lu, Y., Rong, Y., Fang, L., Liu, Y., Han, R. (2017). Characterization of pine-sawdust pyrolytic char activated by phosphoric acid through microwave irradiation and adsorption property toward CDNB in batch mode. Desalination and Water Treatment, 77(7896286): 247-255. https://doi.org/10.5004/dwt.2017.20780

[24] Vinayak, V., Khirade, P.P., Birajdar, S.D., Alange, R.C., Jadhav, K.M. (2015). Electrical and dielectrical properties of low-temperature-synthesized nanocrystalline Mg 2+-substituted cobalt spinel ferrite. Journal of Superconductivity and Novel Magnetism, 28: 3351-3356. https://doi.org/10.1007/s10948-015-3159-6

[25] Liu, Y., Yu, H., Lv, Z., Zhan, S., et al. (2012). Simulated-sunlight-activated photocatalysis of Methylene Blue using cerium-doped SiO_2/TiO_2 nanostructured fibers. Journal of Environmental Sciences, 24(10): 1867-1875. https://doi.org/10.1016/S1001-0742(11)61008-5

[26] Lei, D., Xue, J., Bi, Q., Tang, C., Zhang, L. (2020). 3D/2D direct Z-scheme photocatalyst Zn2SnO4/CdS for simultaneous removal of Cr (VI) and organic pollutant. Applied Surface Science, 517: 146030. https://doi.org/10.1016/j.apsusc.2020.146030

[27] Mohammed, I.T., Haasan, B.A. (2024). Microstructures, morphology and optical properties of Sb2O3: WO3, In2O3 nanostructure composite thin films. Iraqi Journal of Science, 65(10): 5563-5579. https://doi.org/10.24996/ijs.2024.65.10.21

[28] Abdellah, M.H., Nosier, S.A., El-Shazly, A.H., Mubarak, A.A. (2018). Photocatalytic decolorization of methylene blue using TiO_2/UV system enhanced by air sparging. Alexandria Engineering Journal, 57(4): 3727-3735. https://doi.org/10.1016/j.aej.2018.07.018

[29] Dahash, M.S., Ammar, S.H., Abdulnabi, W.A. (2020). Synthesis of magnetic zincoxysulfide core/shell nanocomposites (Ni@ ZnO0.6S0.4) for COD photocatalytic degradation in oil refinery wastewater. IOP Conference Series: Materials Science and Engineering, 928(2): 022063. https://doi.org/10.1088/1757-899X/928/2/022063

[30] Muslim, A.M., Naji, I.S. (2024). Green synthesis of CuO nanoparticles mediated rhazya stricta plant leaves extract characterization and evaluation of their antibacterial and anticancer activity (in vitro Study). Iraqi Journal of Physics, 22(3): 93-105. https://doi.org/10.30723/ijp.v22i3.1259

[31] Li, S., Wang, C., Cai, M., Yang, F., et al. (2022). Facile fabrication of TaON/Bi2MoO6 core–shell S-scheme heterojunction nanofibers for boosting visible-light catalytic levofloxacin degradation and Cr (VI) reduction. Chemical Engineering Journal, 428: 131158. https://doi.org/10.1016/j.cej.2021.131158

[32] Zhang, Z., Wang, W., Wang, L., Sun, S. (2012). Enhancement of visible-light photocatalysis by coupling with narrow-band-gap semiconductor: A case study on Bi2S3/Bi2WO6. ACS Applied Materials & Interfaces, 4(2): 593-597. https://doi.org/10.1021/am2017199

[33] Mirsalari, S.A., Nezamzadeh-Ejhieh, A. (2021). CdS–Ag_3PO_4 nano-catalyst: A brief characterization and kinetic study towards methylene blue photodegradation. Materials Science in Semiconductor Processing, 122: 105455. https://doi.org/10.1016/j.mssp.2020.105455

[34] Ma, M., Yang, Y., Chen, Y., Ma, Y., et al. (2021). Photocatalytic degradation of MB dye by the magnetically separable 3D flower-like Fe_3O_4/SiO_2/MnO_2/BiOBr-Bi photocatalyst. Journal of Alloys and Compounds, 861: 158256. https://doi.org/10.1016/j.jallcom.2020.158256

[35] Arias, M.C., Aguilar, C., Piza, M., Zarazua, E., Anguebes, F., Cordova, V. (2021). Removal of the methylene blue dye (MB) with catalysts of Au-TiO_2: kinetic and degradation pathway. Modern Research in Catalysis, 10(1): 1-14. https://doi.org/10.4236/mrc.2021.101001

[36] Vijayarengan, P., Panchangam, S.C., Stephen, A., Bernatsha, G., et al. (2024). Highly efficient visible light active iron oxide-based photocatalysts for both hydrogen production and dye degradation. Scientific Reports, 14(1): 18299. https://doi.org/10.1038/s41598-024-69413-4

[37] Tareq, M.I., Hasan, B.A. (2024). Micro structures, morphology and optical properties of Sb2O3: WO3, In2O3 nanostructure composite thin films. Iraqi Journal of Science, 65(10): 5563-5579. https://doi.org/10.24996/ijs.2024.65.10.21